Applied Catalysis B: Environmental 265 (2020) 118568

Contents lists available at ScienceDirect

Applied Catalysis B: Environmental

journal homepage: www.elsevier.com/locate/apcatb

Tuning electronic structure of PdZn nanocatalyst via acid-etching strategy for highly selective and stable electrolytic nitrogen fixation under ambient conditions

Min Ma[a], Xiao Han[a], Huiqi Li[a], Xibo Zhang[a], Zhiping Zheng[a], Lingyun Zhou[a], Jun Zheng[b], Zhaoxiong Xie[a,c], Qin Kuang[a,*], Lansun Zheng[a]

[a] State Key Laboratory of Physical Chemistry of Solid Surfaces & Department of Chemistry, College of Chemistry and Chemical Engineering, Xiamen University, Xiamen 361005, Fujian, China
[b] Institute of Physical Science and Information Technology, Anhui University, Hefei 230601, Anhui, China
[c] Pen-Tung Sah Institute of Micro-Nano Science and Technology, Xiamen University, Xiamen 361005, Fujian, China

ARTICLE INFO

Keywords:
Acid-etching technique
Intermetallic PdZn
Electronic structure tuning
Structural defects
Ambient nitrogen reduction reaction catalyst

ABSTRACT

Although ambient nitrogen fixation powered by renewable electricity is emerging as a highly attractive alternative to the classical Haber–Bosch process, it still remains extremely challenging. In this work, a facile acid-etching strategy was employed to synthesize defect-rich PdZn nanoparticles (NPs) supported on N-doped hollow carbon polyhedrons (etched-PdZn/NHCP), which could serve as an attractive and efficient electrocatalyst for the nitrogen reduction reaction (NRR). The synthesized etched-PdZn/NHCP electrocatalyst achieved higher NH_3 yields (5.28 μg $mg_{cat.}^{-1}$ h^{-1}) than pristine PdZn NPs in a phosphate buffer solution. Remarkably, the existence of abundant defects in the etched PdZn NPs favored N_2 adsorption and activation, resulting in significantly high Faradaic efficiency (FE) of 16.9 % towards NH_3 and outperforming previously reported Pd-based NRR electrocatalysts. Furthermore, the etched-PdZn/NHCP cathode exhibited good long-term electrochemical durability with both the NH_3 production and the FE remaining practically stable after 50 h of electrolysis.

1. Introduction

Ammonia (NH_3) as one of the most highly-produced chemicals, appart from a pivotal precursor for nitrogen fertilizer production, is also considered a promising, high-efficiency, and carbon-free energy carrier [1]. Until now, the industrial Haber-Bosch process still dominates the NH_3 manufacture, which involves the coactivation of H_2 and N_2, thereby resulting in a massive consumption of capital and energy [2,3]. These issues can be overcome by the ambient nitrogen reduction reaction (NRR), using water as the hydrogen source. Unfortunately, two significant challenges associated with the electrolytic NRR in aqueous media remain unsolved. On one hand, the high activation barrier for the N≡N triple bond cleavage (940.95 kJ mol^{-1}) results in sluggish reaction kinetics and thus very low NH_3 yields [4,5]. On the other hand, NH_3 is produced with poor selectivities, mostly because of the competitive hydrogen evolution reaction (HER), which takes place readily at 0 V vs. the normal hydrogen electrode [5–7]. Therefore it is highly desirable to explore and develop effective and selective electrocatalysts capable of carrying out electricity-to-ammonia processes under benign conditions.

Recently, it has been reported that carbon-supported Pd nanoparticles (NPs) (Pd/C) could efficiently catalyze the NRR with higher NH_3 production rates (4.5 μg mg_{Pd}^{-1} h^{-1}) than their Au/C and Pt/C counterparts [8]. Computational results have revealed that the outstanding NRR performance of Pd/C could result from the in-situ formation of a palladium hydride (PdH_x) phase at a fixed potential, which not only requires lower free energy for generating *H vacancies (*H-v) with N_2 collision, also being thermodynamically more favorable for creating $*N_2H$ intermediates [8,9]. Although Pd-based compounds were utilized as active cathode catalysts for aqueous NRR [1,4,5,10,11], these electrocatalysts showed poor selectivities for adsorbing and polarizing N_2, resulting in poor Faradic efficiencies (FE, usually below 10 %) toward NH_3. Until now, various effective strategies have been proposed to facilitate the adsorption and activiation of N_2 molecules, such as size/morphology tuning [12,13], heteroatom doping [14,15], defect engineering [16,17], ionic liquid as electrolyte [18,19], et al. Of note, the generation of defects or vacancies in nano-structured catalysts could maximize the intrinsical catalytic ability through tuning its localized

* Corresponding author.
E-mail address: qkuang@xmu.edu.cn (Q. Kuang).

https://doi.org/10.1016/j.apcatb.2019.118568
Received 5 September 2019; Received in revised form 20 December 2019; Accepted 24 December 2019
Available online 25 December 2019
0926-3373/

electronic state, where the electron-rich metal sites could create a energetically favorable binding with target molecules and lower its activiation energy barrier [20]. To the best of our knowledge, study efforts based on defect engineering strategy for applications in ambient NRR are scarce, and still challenging tasks.

Herein, we reported an ambient N_2 fixation route effectively electrocatalyzed over defective PdZn nanoparticles supported on N-doped hollow carbon polyhedrons (etched-PdZn/NHCP), which was synthetized via pyrolysis of a metal organic frameworks (MOFs) precursor followed by an acid-etching procedure. Thanking to the generation of defects (vacancies) in Pd-based nanocatalysts, the etched catalyst could provide sufficient localized electrons to facilitate the chemisorption and synergistic polarization of N_2 molecules, resulting in outstanding electrochemical NRR properties. As expected, the etched-PdZn/NHCP achieved higher NH_3 yields than the corresponding pristine catalyst, with a FE as high as 16.9 %, which outperformed most of the previously reported Pd-based NRR electrocatalysts in aqueous electrolytes.

2. Experimental

2.1. Reagents and materials

Zinc nitrate hexahydrate (Zn $(NO_3)_2{\cdot}6H_2O$), sulfuric acid (H_2SO_4), methanol (CH_3OH), ethanol (C_2H_5OH), ammonium chloride (NH_4Cl), hydrazine hydrate ($N_2H_4{\cdot}H_2O$), KH_2PO_4, $K_2HPO_4{\cdot}3H_2O$, sodium citrate dehydrate ($C_6H_5Na_3O_7{\cdot}2H_2O$) and dimethyl sulphoxide (DMSO) were purchased from Sinopharm Chemical Reagent Co. Ltd. (Shanghai, China). A sodium hypochlorite solution (NaClO), salicylic acid ($C_7H_6O_3$), and 2-methylimidazole were supplied by J.K. Sodium nitroferricyanide dihydrate ($C_5FeN_6Na_2O{\cdot}2H_2O$) was purchased from Xiya Reagent (Shandong, China), while p-dimethylaminobenzaldehyde ($C_9H_{11}NO$) was supplied by Energy Chemical (Shanghai, China). Palladium acetylacetonate ($Pd(acac)_2$) was provided by the Kunming Institute of Precious Metals. Palladium on activated carbon (10 wt%) was purchased from Acros Organics. Ar and high-purity N_2 were obtained from Linde Industrial Gases. The $^{15}N_2$ (^{15}N enrichment of 99 %) gas was purchased from SHANGHAI MAOTOO SPECIAL GAS Co., Ltd. The water used throughout all experiments was ultrapure water.

2.2. Preparation of etched-PdZn/NHCP

ZIF-8 was prepared by following a typical synthesis method. Firstly, 0.6 g of $Zn(NO_3)_2{\cdot}6H_2O$ were dissolved in 25 mL of CH_3OH. A solution consisting of 1.32 g of 2-methylimidazole and 25 mL of CH_3OH was poured into the above Zn-based solution and continuously stirred for 6 h at room temperature. The resulting white product was washed with CH_3OH several times, and vacuum-dried at 60 °C for 24 h. Subsequently, 100 mg of the as-obtained ZIF-8 powder were mixed uniformly with 30 mg of $Pd(acac)_2$ by mechanical lapping. The mixture was placed in a porcelain crucible and heated at 600, 700, and 800 °C for 3 h with a heating rate of 5 °C min^{-1} in an Ar atmosphere, and then naturally cooled to ambient temperature to obtain a series of PdZn samples. The other PdZn samples were also prepared by the pyrolysis of the mixed precursor with a $Pd(acac)_2$/ZIF-8 mass ratio of 10:100 and 20:100 at 600 °C. To prepare etched-PdZn/NHCP, 20 mg of PdZn powder pyrolyzed at 600 °C were evenly dispersed in a 3 M aqueous H_2SO_4 solution and vigorously stirred for 20 h at 60 °C. The final product was obtained by centrifuging with ultrapure water for over ten times before the pH of the supernatant liquid reached 7, followed by vaccum drying at 60 °C for 24 h.

2.3. Preparation of the working electrode

5 mg of catalyst powder were dispersed in mixed solvents containing 500 μL absolute C_2H_5OH, 480 μL water, and 20 μL of a Nafion solution. The mixture was subsequently ultrasonicated for 1 h to form a homogeneous ink. Then, 40 μL of the ink were carefully coated on a carbon paper (1 × 1 cm^2) and the carbon paper with a catalyst loading of 0.2 mg cm^{-2} was dried under ambient conditions.

2.4. Electrochemical measurements

A Nafion membrane was protonated by successively boiling in 5 wt % H_2O_2, water, 5 wt% H_2SO_4, and water for 1 h at 80 °C. This membrane was finally used for separating the two-compartment cells used in this work. Electrochemical measurements were performed with a CHI 650E electrochemical analyzer (CH Instruments, Inc., Shanghai) on a three-electrode system in a 0.1 M PBS solution. Etched-PdZn/NHCP coated on carbon paper was used as the working electrode, while platinum net and a saturated calomel electrode (SCE) served as the counter and the reference electrode, respectively. Before the N_2 reduction test, cyclic voltammetry (CV) was employed to stabilize the catalyst and remove the potential impurities in the working electrode at a scan rate of 50 mV s^{-1}. Moreover, the electrolyte were purged with high-purity N_2 for 30 min, and high-purity N_2 was continuously fed to the cathodic compartment during the test. All measurements were performed under ambient conditions. Otherwise indicated, the potentials reported in this work were recorded versus the reversible hydrogen electrode (RHE), using the following equation: E (RHE) = E (SCE) + (0.242 + 0.059 pH) V.

2.5. Characterizations

X-ray diffraction (XRD) patterns were obtained on a Rigaku Ultima IV diffractometer with Cu Kα radiation (40 KV, 30 mA). Scanning electron microscope (SEM) measurements pictures were recorded on a Hitachi S4800 device at an accelerating voltage of 15 kV. X-ray photoelectron spectroscopy (XPS) data and valence-band (VB) spectra of the samples were collected on an ESCALab 250 X-ray photoelectron spectrometer by using non-monochromatic Al Kα X-ray as the exciting source. Transmission electron microscope (TEM) was performed on a JEOL2100 with an accelerating voltage of 200 kV. The high-angle annular dark-field scanning transmission electron microscopy (HAADF-STEM) and energy-dispersive X-ray (EDX) spectroscopy were performed on an FEI TECNAI F30 microscope at 300 KV. Electron paramagnetic resonance (EPR) data were recorded on a Bruker EMXnano spectrometer. N_2 adsorption–desorption isotherm measurements were performed on a Micromeritics ASAP 2020 M sorptometer. Ultraviolet-visible (UV–vis) spectrophotometry data were measured on a Shimadzu UV-2550. The metal cotents in our samples were determined by inductively coupled plasma optical emission spectrometer (ICP-OES). Before the ICP-OES test, the samples were digested in aqua regia. ^1H nuclear magnetic resonance (^1H NMR) measurements were performed on a Bruker NMR600.

2.6. Determination of NH_3

In this work, the content of NH_3 was spectrophotometrically determined by the indophenol blue method. Specifically, 2 mL of electrolyte were removed from the cathodic chamber and mixed with 2 mL of a 1 M NaOH solution containing 5 wt% $C_7H_6O_3$ and 5 wt% $Na_3C_6H_5O_7{\cdot}2H_2O$. Finally, 1 mL of 0.05 M NaClO and 0.2 mL of the 1 wt % $C_5FeN_6Na_2O$ solution were subsequently added to the above solution. After standing at room temperature in the darkness for 2 h, the absorption spectrum of the reaction solution was measured at a wavelength of 655 nm on an UV–vis spectrophotometer. The concentration-absorbance curve was calibrated using the standard NH_4Cl with different NH_4^+ concentrations in 0.1 M PBS. The fitting curve showed a good linear relationship between the absorbance value and the NH_4^+ concentration. To ensure the accuracy of our experimental data (NH_3 yield rate and FE), we tested the concentration-absorbance standard curve for three times. The production yield of NH_3 was calculated

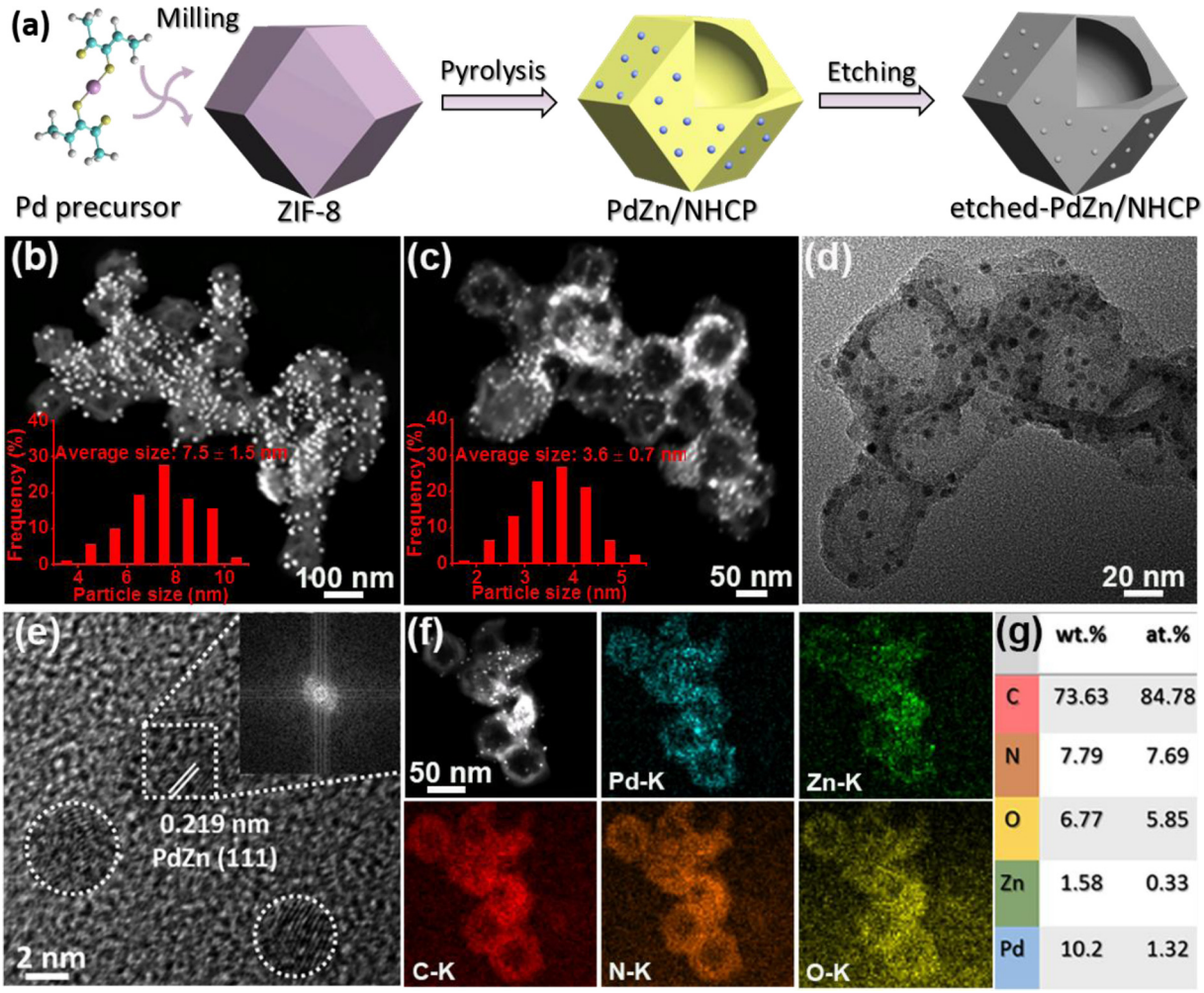

Fig. 1. (a) Schematic illustration of the synthesis process of etched-PdZn/NHCP. HAADF-STEM images for (b) PdZn/NHCP and (c) etched-PdZn/NHCP. The insets are the corresponding particle-size histograms. (d) TEM and (e) HRTEM images of etched-PdZn/NHCP. The inset in (e) is the FFT pattern of the marked white square. (f) EDX elemental mapping images of Pd, Zn, C, N, and O and (g) EDX data of etched-PdZn/NHCP.

according to the Eq. (1):

$$Yieldrate = \frac{V \times C_{NH3}}{t \times m} \quad (1)$$

where C_{NH3} is the measured NH_3 concentration; V is the volume of electrolyte; t is the reduction reaction time; and m is the catalyst loading mass.

2.7. Determination of $N_2H_4{\cdot}H_2O$

The concentration of $N_2H_4{\cdot}H_2O$ in 0.1 M PBS was estimated by the Watt–Chrisp method. To obtain a color reagent, 5.99 g of p-$C_9H_{11}NO$, 30 mL of concentrated HCl, and 300 mL of C_2H_5OH were homogeneously mixed. A series of 5 mL standard $N_2H_4{\cdot}H_2O$ solutions with different concentrations of $N_2H_4{\cdot}H_2O$ in 0.1 M PBS were prepared and separately mixed with 5 mL of the above-mentioned color reagent. After stirring the mixed solution at room temperature in the darkness for 10 min, the absorbance of the reaction solution was measured at a wavelength of at 457 nm. The yield rate of $N_2H_4{\cdot}H_2O$ was calculated according to Eq. (1).

2.8. Calculation of Faradaic efficiency

The Faradaic efficiency for the NRR was defined as the quantity of electric charge used for ammonia synthesis divided by the total charge passed through the electrodes during electrolysis. Assuming that three electrons were needed to produce one NH_3 molecule, the Faradaic efficiency can be calculated as follows (Eq. (2)):

$$Faradaicefficiency = \frac{3F \times V \times C_{NH3}}{17Q} \quad (2)$$

where F is the Faradic constant (96,485 C mol^{-1}); V is the volume of electrolyte; C_{NH3} is the measured NH_3 concentration; and Q is the quantity of applied electricity.

2.9. $^{15}N_2$ isotope labeling experiment

In the $^{15}N_2$ reduction test, PBS electrolyte was firstly bubbled with Ar to remove $^{14}N_2$ (other gas impurities) and fed with $^{15}N_2$ for 30 min. After the 12-h electrolysis on etched-PdZn/NHCP at the applied potential of -0.2 V vs. RHE, 12 mL of electrolyte at the cathodic cell was taken out, and then acidized to pH ~1 with 0.05 M H_2SO_4. A concentrated electrolyte of 2 mL was obtained by heating treatment of aforesaid electrolyte at 70 °C. Subsequently, the resulting solution (0.9 mL) was mixed with 0.1 mL of D_2O containing 50 ppm DMSO, which was served as an internal standard for ^1H NMR measurement.

2.10. Computational details

Spin polarization calculations were carried out by using the Vienna

ab initio simulation package (VASP5.3.3). All the parameters of structural optimization were used the same as our previous work [21]. The D-band center (ε_d) was calculated by using the method developed by Nørskov and co-workers, and given by Eq. (3):

$$\varepsilon_d \frac{\int \rho E dE}{\int \rho dE} \quad (3)$$

Where ρ and E are the density of states (DOS) and energy of electron, respectively. The Pd(111) and PdZn(111) surfaces were modelled by a (2 × 2) supercell with five-layer and ten-layer slabs, respectively.

3. Results and discussion

3.1. Catalyst characterizations

The synthetic process of etched-PdZn/NHCP, which involves the pyrolysis of polyhedral Zn-based MOF (ZIF-8) precursor and subsequent acid-etching treatment, is schematically displayed in Fig. 1a. After pyrolysis of ZIF-8, uniformly distributed PdZn nanoparticles of a tetragonal intermetallic phase (PDF No. 06-0620) were formed on hollow carbon polyhedral matrix and their particle size increased significantly from ca. 7.5 nm to more than 20 nm as the pyrolysis temperature increased from 600 °C to 800 °C (Fig. S1). Moreover, other PdZn samples were prepared by tuning the $Pd(acac)_2$/ZIF-8 mass ratio pyrolyzed at 600 °C, and the related SEM as well as XRD characterizations were displayed in Fig. S2. These samples showed similar-sized alloy nanoparticles with that obtained at the mass ratio of 30:100, but the corresponding hollow carbon polyhedrons suffered from serious aggregations. In general, the reactivity of a nanocatalyst depends on its size [22]. Thus, an optimal catalyst pyrolyzed at 600 °C with the $Pd(acac)_2$/ZIF-8 mass ratio of 30:100 (denoted as PdZn/NHCP) was selected for subsequent etching studies. Note that ZnO was frequently observed around the PdZn NPs in the pyrolyzed sample [23], both phases being together embedded in the carbon matrix (Fig. S3 and S4).

The acid solubility of Zn is higher than that of Pd components based on the knowledge of electrochemistry, so an acid treatment process was implemented on PdZn/NHCP to etch superficial Zn atoms. As shown in Fig. S5, the XRD diffraction peaks of intermetallic PdZn phase gradually weakened with the acid-etching time increased from 12 to 20 h, and no further changes were observed after etching for 24 h. The detailed characterizations of the product after etching for 20 h were provided in this following study. After the acid-etching treatment, the metal NPs remained evenly distributed on the hollow carbon framework, but their sizes decreased from 7.5 nm to 3.6 nm, as revealed by HAADF-STEM and TEM (Fig. 1b–d). The carbon matrix became significantly hollow as a result of the removal of the ZnO particles embedded inside. By comparing the high-resolution TEM (HRTEM) images and corresponding local fast Fourier rransform (FFT) patterns of the etched-PdZn/NHCP and PdZn/NHCP materials (Fig. 1e and Fig. S3), the crystallinity of the metal NPs was found to significantly decrease after etching. This result suggested that the dissolution of Zn components resulted in the appearance of abundant accessible defects or vacancies over the metal NPs. The EDX spectrum and the corresponding elemental mapping images (Figs. 1f and g) confirmed the existence of Pd, Zn, C, N, and O in the etched material, with a Zn/Pd atomic ratio of 1:4. The ICP-OES results (1:4.3) were in line with those of EDX.

The XRD patterns of PdZn/NHCP and etched-PdZn/NHCP are presented in Fig. 2. The diffraction peaks of the ZnO phase completely disappeared and those of the intermetallic PdZn phase significantly weakened after the acid-etching treatement. Accordingly, a very broad peak assigned to amorphous carbon was detected at ca. 26°. Of note, as determined by the EDX and ICP, the Zn/Pd atomic ratio of the etched-PdZn/NHCP was well below that of intermetallic PdZn (1:1), implying that a considerable amount of Zn atoms were removed from the PdZn nanoparticles during the acid-etching process, leaving abundent structural defects.

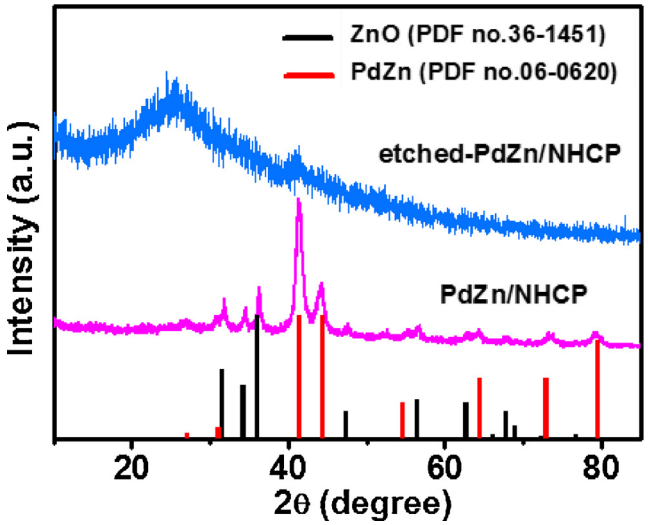

Fig. 2. XRD patterns of etched-PdZn/NHCP and PdZn/NHCP.

To further analyse the compositional changes and the chemical valence of the pyrolysis product during the etching process, the XPS measurements were also carried out on PdZn/NHCP and etched-PdZn/NHCP. According to the XPS survey spectra (Fig. 3a), the intensity of the signals corresponding to Zn were remarkably reduced in the etched sample. The Pd 3d core-level spectra (Fig. 3b) slightly shifted to lower binding energies (BEs) for etched-PdZn/NHCP, which was previously ascribed to the valence band in monometallic Pd having a lower degree of occupancy compared to the intermetallic compound [24,25]. That's to say, the lower BE of the Pd 3d region could be caused by the lower Zn contents of the PdZn. The other two peaks at 337.9 and 343.6 eV were assigned to highly oxidized Pd species formed by exposure to air, which indirectly represents the high activity of defective PdZn NPs [23]. The intensity of the Zn 2p signals in the etched-PdZn/NHCP material significantly decreased and shifted to lower BEs as compared to the prystine material (Fig. 3c), which was attributed to the removal of ZnO phase during the acid treatment. Of note, the deconvolution of the high-resolution O 1s spectra for the two samples revealed a significantly lower content of lattice oxygen (O_L) species (BE of 530.7 eV) for the etched material, which mainly arised from ZnO (Fig. 3d). In contrast, the amounts of oxygen vacancies (O_V) and chemisorbed O species (O_C) at ca. 531.6 and 532.5 eV, respectively, significantly increased in the etched material. These results confirmed the onset of structual defects on the our samples after acid-etching, thus advantageously adsorbing N_2 molecule and selectively favoring the NRR process [23,26]. Interestingly, a strong signal ascribed to thermally unstable pyrrolic N appeared in the etched product (Fig. S6), although the effect of these species on the NRR activity was negligible [27,28].

EPR was conducted to further identify the presence of defects in our samples (Fig. 4). The etched-PdZn/NHCP showed a stronger characteristic signal at nearly g = 2.003 compared to PdZn/NHCP, and the g-factor was very closed to that of free electrons at 2.0021 [29]. It should be stated that single ionized zinc vacancies and oxygen vacancies were hardly distinguished since they have almost identical g values [23,30,31]. The higher EPR signal could be attributed to unpaired electrons being strongly captured by zinc or oxygen vacancies in our etched sample. To measure the Brunauer–Emmett–Teller (BET) specific surface areas of the two samples, N_2 adsorption–desorption isotherms were also recorded. As show in Fig. S7, both samples exhibited typical type-IV isotherms, generally associated with capillary condensation in mesopore structures, with a well-defined H4 hysteresis loop [32,33]. The analytic data revealed the etched-PdZn/NHCP (367.4 $m^2\ g^{-1}$) had larger BET specific surface area than PdZn/NHCP (224.4

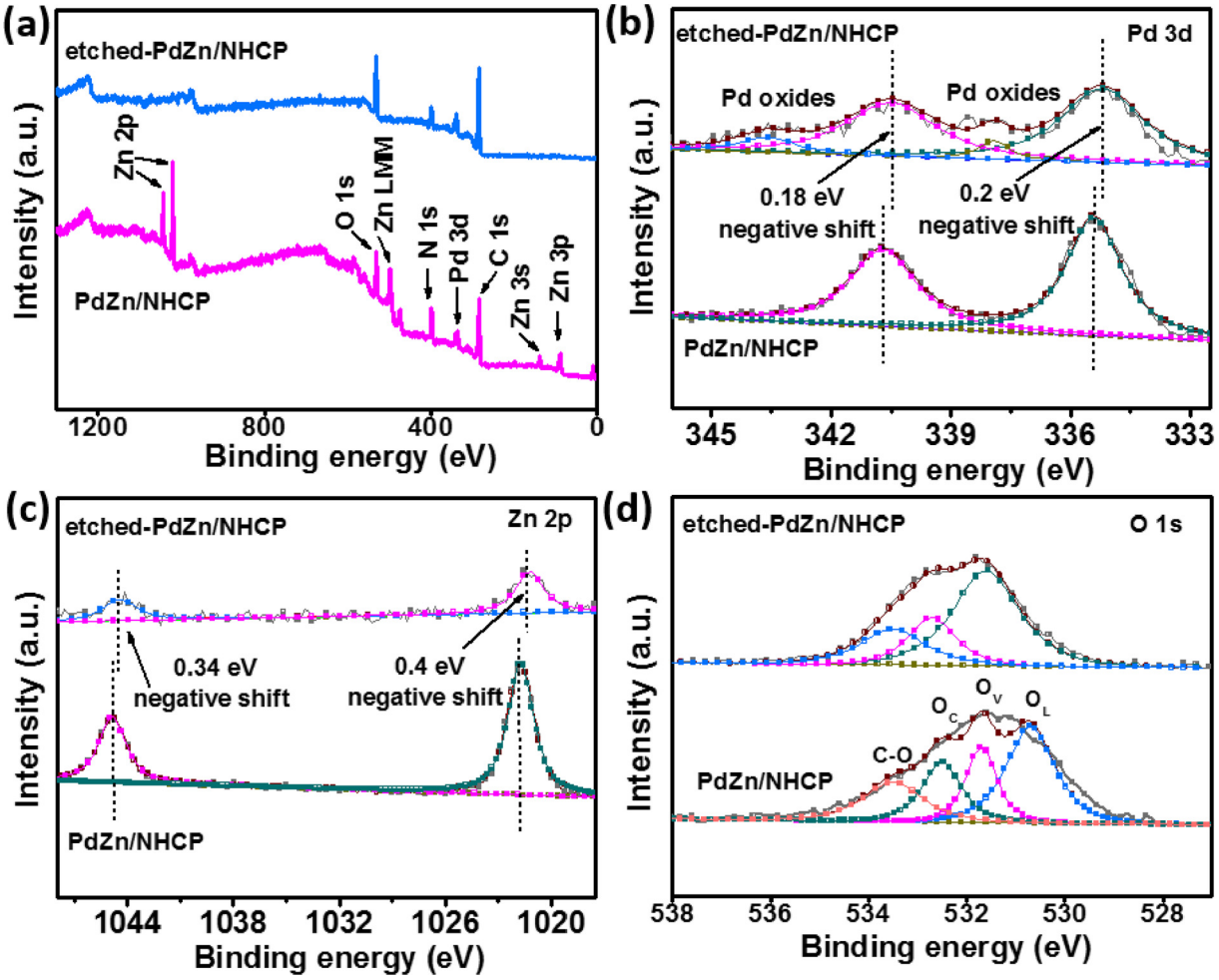

Fig. 3. (a) XPS survey spectra of etched-PdZn/NHCP and PdZn/NHCP. The XPS spectra of two samples in the (b) Pd 3d, (c) Zn 2p, and (d) O 1s regions.

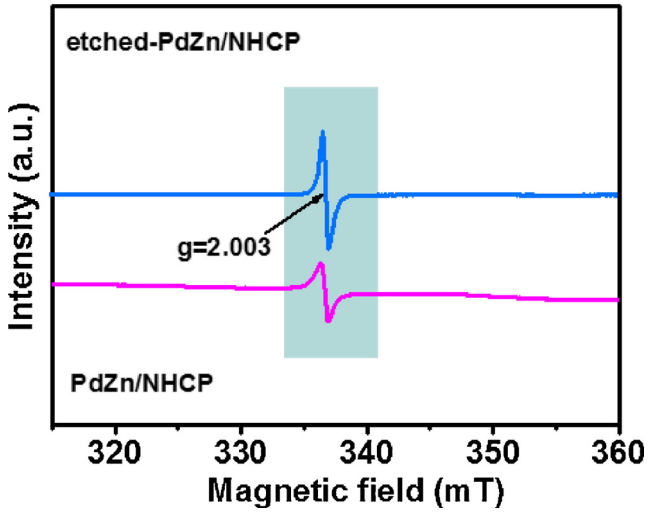

Fig. 4. EPR spectra of etched-PdZn/NHCP and PdZn/NHCP.

$m^2\ g^{-1}$) as a result of the removal of ZnO particles embedded inside, thus boosting charge and mass transport and improving the NRR behavior.

In order to well understand the role of Zn component within PdZn alloy, we calculated the DOS of Pd (111) and PdZn (111), and obtained the corresponding D-band center by the traditional calculation [34]. As shown in Fig. S8, the D-band center of PdZn (111) shifted far from Fermi level compared to Pd (111), implying the electron donation from the Pd to Zn [35,36]. Also, the XPS VB spectra of etched-PdZn/NHCP and commercial Pd/C were collected, as shown in Fig. S9. The D-band centers derived from VB spectra were quantified according to previous work [37], and it also showed a downshift of D-band center for etched-PdZn/NHCP (-3.33 eV) than commercial Pd/C (-2.53 eV). Both theoretical and experimental results demonstrated the effect on the electronic structure of Pd by alloying Zn. It can be expected to balance the binding of catalyst materials with target molecules (N_2 and NH_3), allowing for the optimization of NRR performance on etched-PdZn/NHCP [36,38].

3.2. Electrochemical performances

The electrocatalytic NRR activities of all samples loaded on hydrophobic carbon paper (1 × 1 cm^2) were tested on a gas-tight two-compartment cell with a N_2-saturated 0.1 M PBS as an electrolyte (pH = 7.0) under ambient conditions. The linear sweep voltammetry (LSV) curves of etched-PdZn/NHCP were measured in N_2- or Ar-saturated PBS solutions (Fig. S10). Both curves showed similar profiles, with a higher current density for the curve in the N_2-saturated electrolyte. These results indicated that etched-PdZn/NHCP can effectively catalyze the NRR at a starting potential of —0.1 V. Accordingly, the chronoamperometric curves for 2 h electrolysis were obtained at different applied potentials (Fig. S11). The concentrations of NH_3 in the electrolyte were detected by the indophenol blue method (Fig. S12), which has a low detection limit and good reproducibility [39]. As shown in Fig. 5a and b, the maximum absorbance was achieved at the applied

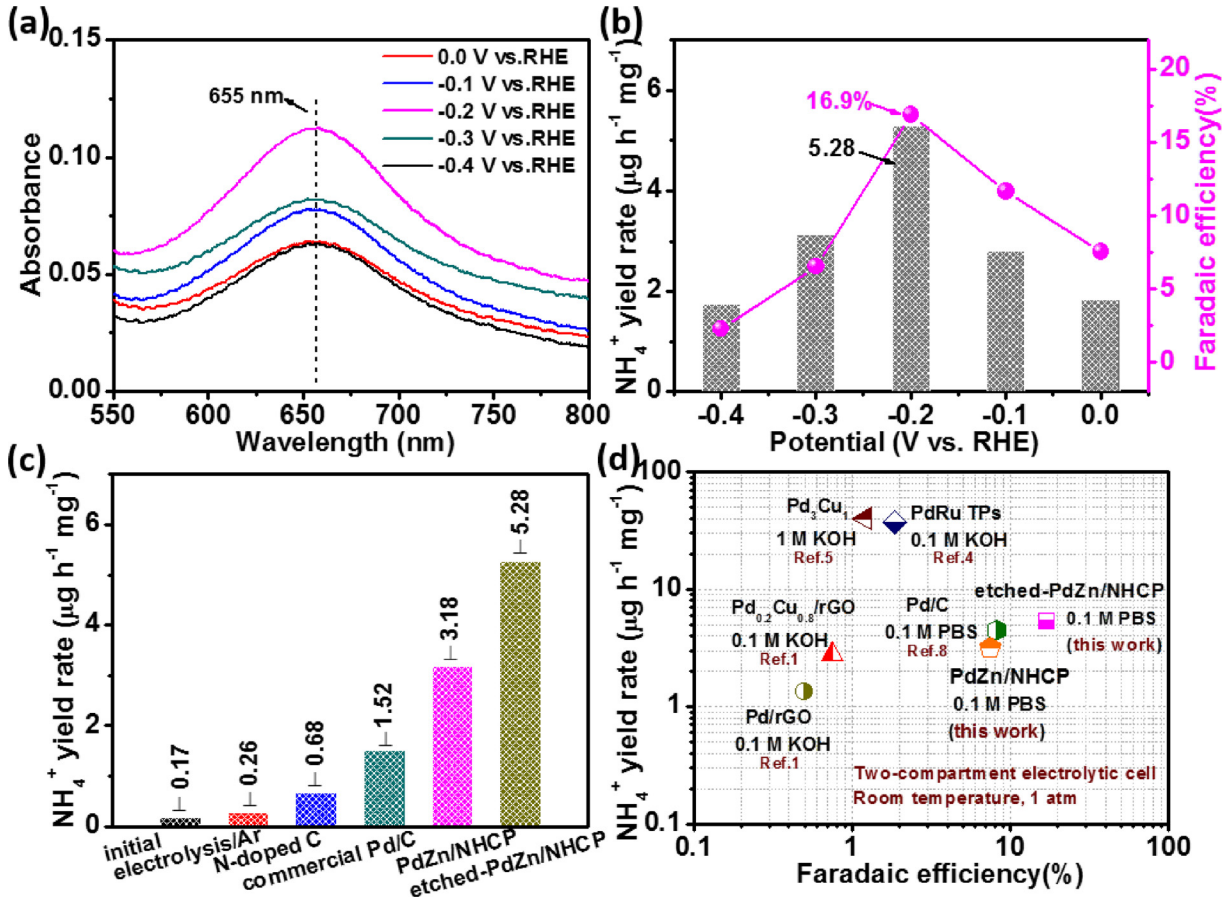

Fig. 5. (a) UV–vis absorption spectra of the electrolytes after electrolysis and (b) corresponding NH_3 yield rates and FEs of etched-PdZn/NHCP at different fixed potentials. (c) Yield rates for the different catalysts tested herein. (d) Comparisons of the yield rates and FEs for etched-PdZn/NHCP with other reported works.

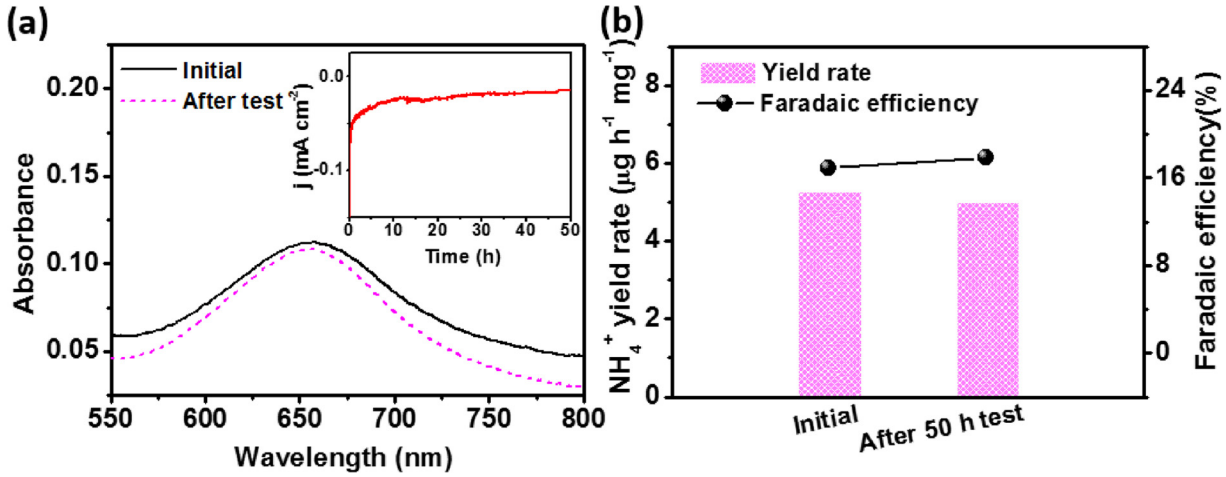

Fig. 6. (a) The UV–vis absorption spectra of the electrolytes and (b) corresponding yield rates and FEs before and after the stability test. The inset in (a) represents the chronoamperometric plot at the potential of −0.2 V.

potential of —0.2 V, at which an optimal NH_3 production of 5.28 μg $mg_{cat.}^{-1}$ h^{-1} was obtained. Meanwhile, the etched-PdZn/NHCP had the best FE value of 16.9 % at —0.2 V. Weaker absorbance responses were obtained at voltages below —0.2 V, revealing poorer NRR performances, which is explained by significantly improved HER at these potentials. Some control experiments were performed to confirm the origin of the produced NH_3. Very low amount of NH_3 was detected in the blank and Ar-saturated electrolyte, and the pure ZIF-8-derived N-doped carbon and commercial Pd/C showed poor NRR activity, as reveled by Fig. 5c and Figs. S13-14. The $^{15}N_2$ isotope labeling experiment was also conducted to find out where our NH_3 was originated from (see Experimental section for tested details). As observed by ^1H NMR spectra (Fig. S15), the $^{14}N_2$-feeding electrolyte had a triplet coupling for $^{14}NH_4^+$ while $^{15}N_2$-feeding electrolyte principally showed a doublet coupling characteristics of $^{15}NH_4^+$. When the electrolyte was bubbled with Ar, no apparent signals were detected in post-electrolysis products, excluding the possibility of N source directly leaching from working electrode. The existence of minor $^{14}NH_4^+$ in $^{15}N_2$-feeding

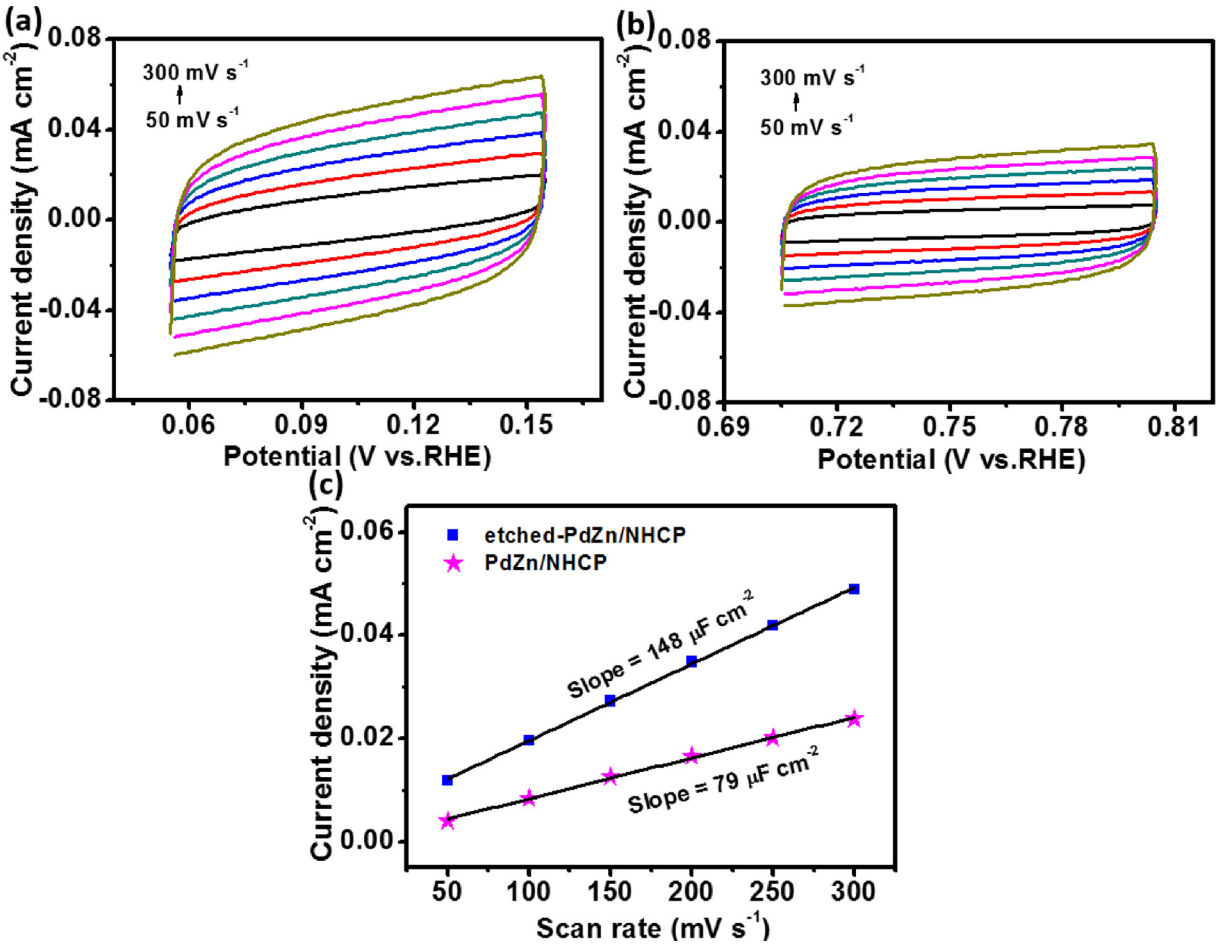

Fig. 7. Cyclic voltammograms for (a) etched-PdZn/NHCP and (b) PdZn/NHCP in the non-Faradic capacitance current range at scan rates of 50, 100, 150, 200, 250, and 300 mV s^{-1} in 0.1 M PBS. (c) Capacitive currents versus scan rates for two catalysts.

products could be interpreted in this way: the N components in our etched-PdZn/NHCP could be involved in the NRR process via Mars-van Krevelen mechanism when the external N_2 was continuously supplied to electrolyte [28,40]. Even so, the NH_3 collected in our experiments was mainly derived from the electroreduction of feeding gas on the etched-PdZn/NHCP because the obtained $^{15}NH_4^+$ yield rate value in $^{15}N_2$-saturated electrolyte by integrating the peak area of ^1H NMR spectra was closed to 5.28 μg $mg_{cat.}^{-1}$ h^{-1}. Additionally, the bad NRR behavior on Zn/N-doped C synthesized by directly pyrolyzing ZIF-8 verified that this electroreduction process occurred at Pd centres rather than Zn centres (Fig. S16). Impressively, the etched catalyst showed a higher NRR activity than PdZn/NHCP (3.18 μg $mg_{cat.}^{-1}$ h^{-1}) (Fig. S17). The remarkable FE of 16.9 % represents one of the best performance among previously reported Pd-based catalysts (Fig. 5d), and more comparisons of NRR performances with recently reported non-noble metals based electrocatalysts working in the aqueous electrolyte were listed in Table S1. The cycling stability of etched-PdZn/NHCP was evaluated by performing continuous NRR electrolysis for 5 times (10 h) at the potential of -0.2 V vs. RHE, and no obvious changes in both NH_3 yield rate and FE were found (Fig. S18). To investigate the long-term durability of the etched catalyst, bulk electrolysis was carried out for 50 h at the fixed potential of —0.2 V. An insignificant loss in current density was observed, revealing a robust stability for the NRR process. Besides, the NH_3 yield rate and FE remained nearly unchanged before and after the electrolysis (Figs. 6a and b). After stability test, the TEM and HAADF-STEM images of etched-PdZn/NHCP were collected in Fig. S19, indicating that PdZn nanoparticles were still uniformly distributed on NHCP, and the carbon polyhedron was stable for at least 50 h. Interestingly, the vacancy defects were still detected in the etched-PdZn/NHCP, as revealed by EPR data (Fig. S20). The EPR signal decreased compared with that for the etched-PdZn/NHCP before test, possibly because defect sites were destroyed partially and the amount for measured sample was smaller.

The catalytic activity of electrocatalysts depends strongly on the electrochemical surface area (ECSA), which is reflected by the specific double-layer capacitance (C_{DL}) at the electrode/electrolyte interface. The C_{DL} was obtained by CV based on a previous report [41]. Fig. 7a and b show the cyclic voltammograms of the etched-PdZn/NHCP and PdZn/NHCP, respectively. The C_{DL} was determined by this formula: $i_c = \nu \times C_{DL}$. That is to say, the slope of the linear relationship between capacitive current (i_c) and scan rate (ν) of the cyclic voltammogram curve is the C_{DL}. As presented in Fig. 7c, the etched-PdZn/NHCP showed a much higher C_{DL} than PdZn/NHCP. Thus, the former catalyst had a higher ECSA, which is benefitial for effective nitrogen reduction catalysis.

A possible $N_2H_4{\cdot}H_2O$ intermediate was further determined spectrophotometrically by the Watt–Chrisp method [42], and the related detection calibration curves are presented in Fig. S21. Poor $N_2H_4{\cdot}H_2O$ production was obtained, revealing an outstanding selectivity to NH_3 over etched-PdZn/NHCP. According to previous studies, the ambient NRR over our etched-PdZn/NHCP should follow an associative distal mechanism (Fig. 8a) [43]. Based on the aforementioned analyses, we proposed a feasible reaction pathway for NH_3 synthesis on etched-PdZn/NHCP material. When the etched-PdZn/NHCP contacted with N_2-saturated PBS aqueous solution, the Pd sites can favorably capture the activated H* to simulate PdH_x phase at the applied potential, and

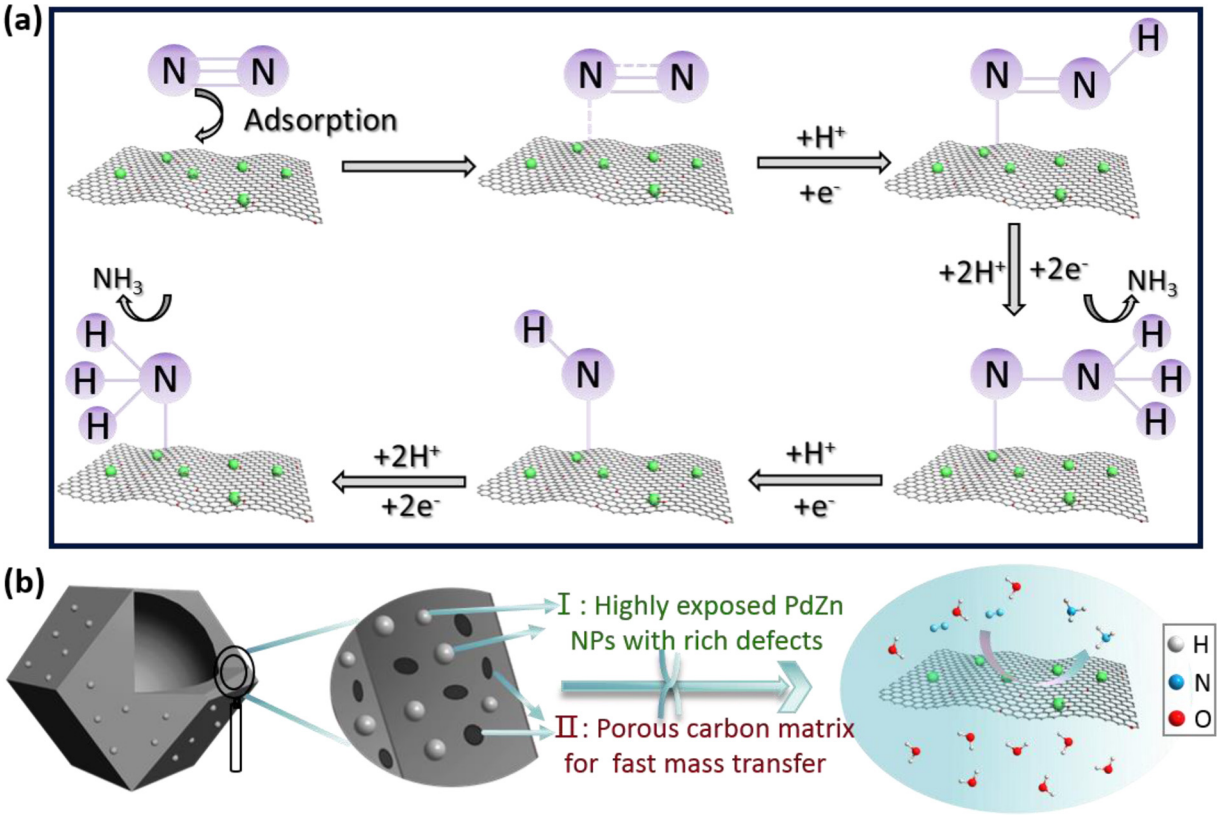

Fig. 8. (a) Distal hydrogenation pathway for electrochemical NRR on etched-PdZn/NHCP under ambient conditions. (b) Schematic illustration of the etched-PdZn/NHCP electrode for efficient NRR catalysis.

simultaneously the electron-rich sites induced by vacancy defects had a strong binding with dissolved N_2 to activate its triple bond [8,20,44]. Then, the distal N atom of adsorbed N_2 preferentially initiated the hybrydizing reaction with activated H* from the electrolyte to form a more stable N−H bond on PdH_x and the initial N≡N bond was broken. Ultimately, successive hydrogenation processes occurred until forming the first NH_3 molecule, after which the neighbour N atom was gradually transformed into another NH_3 molecule [10,45]. Such reaction process on etched-PdZn/NHCP was more dynamically achievable because of the decreased transport distance between adsorbed N_2 and H*, and it proceeded repeatedly until the NRR electrolysis was terminated. Simultaneously, the production of NH_3 was driven by N elements in etched-PdZn/NHCP via Mars-van Krevelen mechanism. In this study, the structural and morphological advantages of our etched-PdZn/NHCP sample were favorable for carrying out the electrocatalytic NRR (Fig. 8b). On one hand, the hollow N-doped carbon network obtained by pyrolysis of ZIF-8 can supply sufficiently open spaces to facilitate electron transport and electrolyte penetration. The pyrolysed carbon matrix-supported PdZn particles ensured high exposure and accessibility to N_2 molecules. On the other hand, the entire ZnO and the primary Zn component of PdZn alloy were removed by the acid solution, generating a surface-rough and defective nanostructure with a lower particle size. This locally induced electron-rich feature of the etched-PdZn/NHCP was mostly responsible for the capture and synergistic activation of dissolved N_2, which is very important for selectively catalyzing NRR under ambient conditions.

4. Conclusions

In summary, a delicate hybrid catalyst with defective PdZn NPs anchored on a NHCP matrix was successfully fabricated via facile acid-etching on a MOF-derived pyrolysis product. This material was efficient in catalyzing the NRR in neutral PBS. Strikingly, the obtained catalyst exhibited a notable selectivity to NH_3 with a high FE of 16.9 %, which is far superior to those of previously most reported Pd-based catalysts. Experimental studies confirmed that vacancy defects were generated in the catalysts, increasing available charge density. These sites played a pivotal role in promoting N_2 molecule capture and hydrogenation, hence achieving a satisfactory NRR ability whilst effectively hindering the HER. The utilization of a carbon support with intrinsically strong acid-base resistance made etched-PdZn/NHCP a robust NRR cathode material, with almost no loss in activity after 50 h of electrolysis. This work offers us a high-selective and durable NRR electrocatalysts working under mild conditions. More significantly, this work proposes a new strategy to greatly improve the NRR performance of nano-structured alloy electrocatalysts for practical applications.

Credit author statement

Q. Kuang and Z.X. Xie proposed the research project and guided the whole experiments. L.S. Zheng gave important advice on the research project. M. Ma conducted the syntheses and characterization of the PdZn nanocatalyst, and drafted the manuscript. X. Han, H. Q. Li, and X. B. Zhang provided help in electrochemical measurement. Z. P. Zheng and J. Zheng provided help in TEM and XPS characterization, respectively. L. Y. Zhou conducted the theoretical calculations and analyses.

Declaration of Competing Interest

The authors declare that they have no known competing financial interests or personal relationships that could have appeared to influence the work reported in this paper.

Acknowledgements

This work was supported by the National Key Research and

Development Program of China (2017YFA0206500 and 2017YFA0206801), the National Basic Research Program of China (2015CB932301), and the National Natural Science Foundation of China (21671163, 21773190, 21721001, and 21931009). We thank Liubin Feng in Xiamen University for help in the NMR measurement.

Appendix A. Supplementary data

Supplementary material related to this article can be found, in the online version, at doi:https://doi.org/10.1016/j.apcatb.2019.118568.

References

[1] M.-M. Shi, D. Bao, S.-J. Li, B.-R. Wulan, J.-M. Yan, Q. Jiang, Anchoring PdCu amorphous nanocluster on graphene for electrochemical reduction of N_2 to NH_3 under ambient conditions in aqueous solution, Adv. Energy Mater. 8 (2018) 1800124.
[2] D. Bao, Q. Zhang, F.-L. Meng, H.-X. Zhong, M.-M. Shi, Y. Zhang, J.-M. Yan, Q. Jiang, X.-B. Zhang, Electrochemical reduction of N_2 under ambient conditions for artificial N_2 fixation and renewable energy storage using N_2/NH_3 cycle, Adv. Mater. 29 (2017) 1604799.
[3] W. Guo, Z. Liang, J. Zhao, B. Zhu, K. Cai, R. Zou, Q. Xu, Hierarchical cobalt phosphide hollow nanocages toward electrocatalytic ammonia synthesis under ambient pressure and room temperature, Small Methods 2 (2018) 1800204.
[4] H. Wang, Y. Li, C. Li, K. Deng, Z. Wang, Y. Xu, X. Li, H. Xue, L. Wang, One-pot synthesis of bi-metallic PdRu tripods as an efficient catalyst for electrocatalytic nitrogen reduction to ammonia, J. Mater. Chem. A 7 (2019) 801–805.
[5] F. Pang, Z. Wang, K. Zhang, J. He, W. Zhang, C. Guo, Y. Ding, Bimodal nanoporous Pd_3Cu_1 alloy with restrained hydrogen evolution for stable and high yield electrochemical nitrogen reduction, Nano Energy 58 (2019) 834–841.
[6] J. Deng, J.A. Íñiguez, C. Liu, Electrocatalytic nitrogen reduction at low temperature, Joule 2 (2018) 846–856.
[7] A.R. Singh, B.A. Rohr, J.A. Schwalbe, M. Cargnello, K. Chan, T.F. Jaramillo, I. Chorkendorff, J.K. Norskov, Electrochemical ammonia synthesis-the selectivity challenge, ACS Catal. 7 (2017) 706–709.
[8] J. Wang, L. Yu, L. Hu, G. Chen, H. Xin, X. Feng, Ambient ammonia synthesis via palladiumcatalyzed electrohydrogenation of dinitrogen at low overpotential, Nat. Commun. 9 (2018) 1795.
[9] D. Gao, H. Zhou, F. Cai, D. Wang, Y. Hu, B. Jiang, W.-B. Cai, X. Chen, R. Si, F. Yang, S. Miao, J. Wang, G. Wang, X. Bao, Switchable CO_2 electroreduction via engineering active phases of Pd nanoparticles, Nano Res. 10 (2017) 2181–2191.
[10] J. Lv, S. Wu, Z. Tian, Y. Ye, J. Liu, C. Liang, Construction of PdO-Pd interfaces assisted by laser irradiation for enhanced electrocatalytic N_2 reduction reaction, J. Mater. Chem. A 7 (2019) 12627–12634.
[11] H. Wang, Y. Li, D. Yang, X. Qian, Z. Wang, Y. Xu, X. Li, H. Xue, L. Wang, Direct fabrication of bi-metallic PdRu nanorod assemblies for electrochemical ammonia synthesis, Nanoscale 11 (2019) 5499–5505.
[12] Z. Geng, Y. Liu, X. Kong, P. Li, K. Li, Z. Liu, J. Du, M. Shu, R. Si, J. Zeng, Achieving a record-high yield rate of 120.9 μg_{NH3} $mg_{cat.}^{-1}$ h^{-1} for N_2 electrochemical reduction over Ru single-atom catalysts, Adv. Mater. 30 (2018) 1803498.
[13] L. Han, X. Liu, J. Chen, R. Lin, H. Liu, F. Lü, S. Bak, Z. Liang, S. Zhao, E. Stavitski, J. Luo, R.R. Adzic, H.L. Xin, Atomically dispersed molybdenum catalysts for efficient ambient nitrogen fixation, Angew. Chem. Int. Ed. 58 (2019) 2321–2325.
[14] W. Qiu, X.-Y. Xie, J. Qiu, W.-H. Fang, R. Liang, X. Ren, X. Ji, G. Cui, A.M. Asiri, G. Cui, B. Tang, X. Sun, High-performance artificial nitrogen fixation at ambient conditions using a metal-free electrocatalyst, Nat. Commun. 9 (2018) 3485.
[15] X. Mao, S. Zhou, C. Yan, Z. Zhu, A. Du, A single boron atom doped boron nitride edge as a metal-free catalyst for N_2 fixation, Phys. Chem. Chem. Phys. 21 (2019) 1110–1116.
[16] H. Tao, C. Choi, L.-X. Ding, Z. Jiang, Z. Han, M. Jia, Q. Fan, Y. Gao, H. Wang, A.W. Robertson, S. Hong, Y. Jung, S. Liu, Z. Sun, Nitrogen fixation by Ru single-atom electrocatalytic reduction, Chem 5 (2019) 204–214.
[17] Y. Zhang, W. Qiu, Y. Ma, Y. Luo, Z. Tian, G. Cui, F. Xie, L. Chen, T. Li, X. Sun, High-performance electrohydrogenation of N_2 to NH_3 catalyzed by multishelled hollow Cr_2O_3 microspheres under ambient conditions, ACS Catal. 8 (2018) 8540–8544.
[18] F. Zhou, L.M. Azofra, M. Ali, M. Kar, A.N. Simonov, C. McDonnell-Worth, C. Sun, X. Zhang, D.R. MacFarlane, Electro-synthesis of ammonia from nitrogen at ambient temperature and pressure in ionic liquids, Energy Environ. Sci. 10 (2017) 2516–2520.
[19] G.-F. Chen, X. Cao, S. Wu, X. Zeng, L.-X. Ding, M. Zhu, H. Wang, Ammonia electrosynthesis with high selectivity under ambient conditions via a Li^+ incorporation strategy, J. Am. Chem. Soc. 139 (2017) 9771–9774.
[20] Y. Wang, M.-M. Shi, D. Bao, F.-L. Meng, Q. Zhang, Y.-T. Zhou, K.-H. Liu, Y. Zhang, J.-Z. Wang, Z.-W. Chen, D.-P. Liu, Z. Jiang, M. Luo, L. Gu, Q.-H. Zhang, X.-Z. Cao, Y. Yao, M.-H. Shao, Y. Zhang, X.-B. Zhang, J.G. Chen, J.-M. Yan, Q. Jiang, Generating defect-rich bismuth for enhancing rate of nitrogen electroreduction to ammonia, Angew. Chem. Int. Ed. 58 (2019) 9464–9469.
[21] X. Zhao, L. Zhou, W. Zhang, C. Hu, L. Dai, L. Ren, B. Wu, G. Fu, N. Zheng, Thiol treatment creates selective palladium catalysts for semihydrogenation of internal alkynes, Chem 4 (2018) 1080–1091.
[22] M. Hu, S. Zhao, S. Liu, C. Chen, W. Chen, W. Zhu, C. Liang, W.-C. Cheong, Y. Wang, Y. Yu, Q. Peng, K. Zhou, J. Li, Y. Li, MOF-confined sub-2 nm atomically ordered intermetallic PdZn nanoparticles as high-performance catalysts for selective hydrogenation of acetylene, Adv. Mater. 30 (2018) 1801878.
[23] Y. Yin, B. Hu, X. Li, X. Zhou, X. Hong, G. Liu, Pd@zeolitic imidazolate framework-8 derived PdZn alloy catalysts for efficient hydrogenation of CO_2 to methanol, Appl. Catal. B 234 (2018) 143–152.
[24] S. Furukawa, M. Endo, T. Komatsu, Bifunctional catalytic system effective for oxidative dehydrogenation of 1-butene and n-butane using Pd-based intermetallic compounds, ACS Catal. 4 (2014) 3533–3542.
[25] M. Friedrich, D. Teschner, A. Knop-Gericke, M. Armbrüster, Influence of bulk composition of the intermetallic compound ZnPd on surface composition and methanol steam reforming properties, J. Catal. 285 (2012) 41–47.
[26] M. Samadi, H.A. Shivaee, A. Pourjavadi, A.Z. Moshfegh, Synergism of oxygen vacancy and carbonaceous species on enhanced photocatalytic activity of electrospun ZnO-carbon nanofibers: Charge carrier scavengers mechanism, Appl. Catal. A 466 (2013) 153–160.
[27] Y. Liu, Y. Su, X. Quan, X. Fan, S. Chen, H. Yu, H. Zhao, Y. Zhang, J. Zhao, Facile ammonia synthesis from electrocatalytic N_2 reduction under ambient conditions on N-doped porous carbon, ACS Catal. 8 (2018) 1186–1191.
[28] S. Mukherjee, D.A. Cullen, S. Karakalos, K. Liu, H. Zhang, S. Zhao, H. Xue, K.L. More, G. Wang, G. Wu, Metal-organic framework-derived nitrogen-doped highly disordered carbon for electrochemical ammonia synthesis using N_2 and H_2O in alkaline electrolytes, Nano Energy 48 (2018) 217–226.
[29] B. Yu, C. Zhu, F. Gan, Y. Huang, Electron spin resonance properties of ZnO microcrystallites, Mater. Lett. 33 (1998) 247–250.
[30] Y. Li, S. Zhou, Y. Li, K. Sharafudeen, Z. Ma, G. Dong, M. Peng, J. Qiu, Long persistent and photo-stimulated luminescence in Cr^{3+}-doped Zn-Ga-Sn-O phosphors for deep and reproducible tissue imaging, J. Mater. Chem. C 2 (2014) 2657–2663.
[31] H. Kaftelen, K. Ocakoglu, R. Thomann, S. Tu, S. Weber, E. Erdem, EPR and photoluminescence spectroscopy studies on the defect structure of ZnO nanocrystals, Phys. Rev. B 86 (2012) 014113.
[32] Z. Qi, Y. Pei, T. Wei Goh, Z. Wang, X. Li, M. Lowe, R.V. Maligal-Ganesh, W. Huang, Conversion of confined metal@ZIF-8 structures to intermetallic nanoparticles supported on nitrogen-doped carbon for electrocatalysis, Nano Res. 11 (2018) 3469–3479.
[33] J. Zhang, Y. Wang, K. Xiao, S. Cheng, T. Zhang, G. Qian, Q. Zhang, Y. Feng, N-Doped hierarchically porous carbon derived from heterogeneous core-shell ZIF-L (Zn)@ZIF-67 for supercapacitor application, New J. Chem. 42 (2018) 6719–6726.
[34] B. Hammer, J.K. Nørskov, Theoretical surface science and catalysis—calculations and concepts, Adv. Catal. (45) (2000) 71–129.
[35] Z.-X. Chen, K.M. Neyman, A.B. Gordienko, N. Rösch, Surface structure and stability of PdZn and PtZn alloys: Density-functional slab model studies, Phys. Rev. B 68 (2003) 075417.
[36] S. Hu, F. Che, B. Khorasani, M. Jeon, C. Won Yoon, J.-S. McEwen, L. Scudiero, S. Ha, Improving the electrochemical oxidation of formic acid by tuning the electronic properties of Pd-based bimetallic nanoparticles, Appl. Catal. B 254 (2019) 685–692.
[37] X. Li, X. Wang, M. Liu, H. Liu, Q. Chen, Y. Yin, M. Jin, Construction of Pd-M (M = Ni, Ag, Cu) alloy surfaces for catalytic applications, Nano Res. 11 (2018) 780–790.
[38] W. Tong, B. Huang, P. Wang, L. Li, Q. Shao, X. Huang, Crystal-phase-engineering enabled PdCu electrocatalyst for enhanced ammonia synthesis, Angew. Chem. Int. Ed. (2019) doi.10.1002/anie.201913122.
[39] D. Zhu, L. Zhang, R.E. Ruther, R.J. Hamers, Photo-illuminated diamond as a solid-state source of solvated electrons in water for nitrogen reduction, Nat. Mater. 12 (2013) 836–841.
[40] Y. Abghoui, E. Skúlason, Onset potentials for different reaction mechanisms of nitrogen activation to ammonia on transition metal nitride electro-catalysts, Catal. Today 286 (2017) 69–77.
[41] C.C. Mccrory, S. Jung, J.C. Peters, T.F. Jaramillo, Benchmarking heterogeneous electrocatalysts for the oxygen evolution reaction, J. Am. Chem. Soc. 135 (2013) 16977–16987.
[42] G.W. Watt, J.D. Chrisp, Spectrophotometric method for determination of hydrazine, Anal. Chem. 24 (1952) 2006–2008.
[43] X. Cui, C. Tang, Q. Zhang, A review of electrocatalytic reduction of dinitrogen to ammonia under ambient conditions, Adv. Energy Mater. 8 (2018) 1800369.
[44] G. Zhang, Q. Ji, K. Zhang, Y. Chen, Z. Lie, H. Liu, J. Li, J. Qu, Triggering surface oxygen vacancies on atomic layered molybdenum dioxide for a low energy consumption path toward nitrogen fixation, Nano Energy 59 (2019) 10–16.
[45] N. Cao, G. Zheng, Aqueous electrocatalytic N_2 reduction under ambient conditions, Nano Res. 11 (2018) 2992–3008.